



# Investigation of ROS scavenging properties and in vitro cytotoxicity of oxygen-deficient $\text{La}_2\text{O}_{3-x}$ nanostructure synthesized by spray pyrolysis method

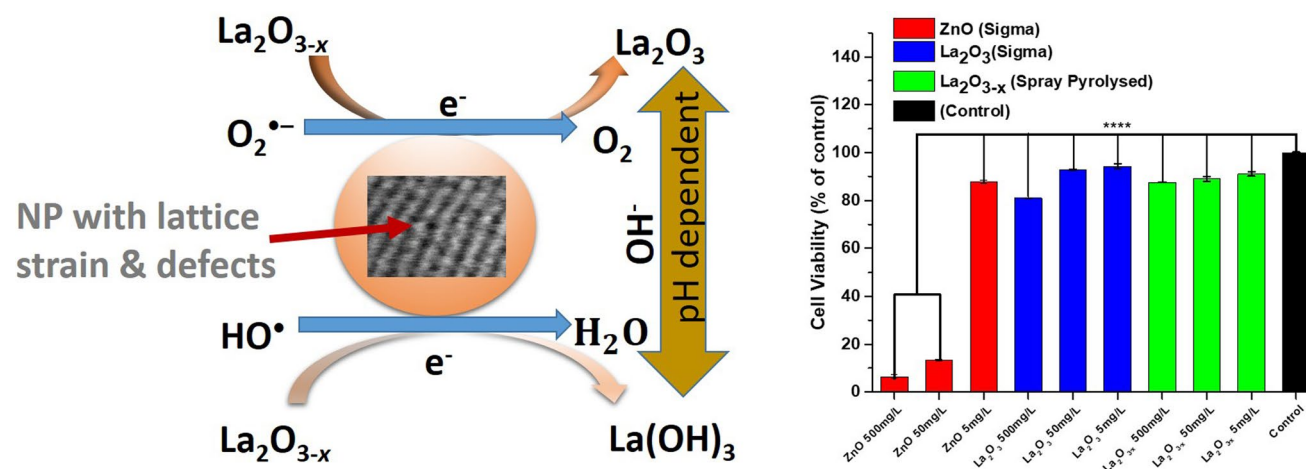
Yaser Rehman<sup>1</sup> · Corentin Copet<sup>2</sup> · Alexander Morlando<sup>1</sup> · Xu-Feng Huang<sup>3</sup> · Konstantin Konstantinov<sup>1</sup>

Received: 11 July 2020 / Accepted: 20 September 2020 / Published online: 9 October 2020  
© Islamic Azad University 2020

## Abstract

Oxygen-deficient metal oxides have seen increased application in the field of free radical biology, whereby their electronic structure imparts unique antioxidant properties. In this work, we use the facile, one-step, cost-effective method of spray pyrolysis to synthesize oxygen-deficient lanthanum oxide ( $\text{La}_2\text{O}_{3-x}$ ), nanoparticles. Structural and morphological characterization revealed the formation of an aggregate of  $\text{La}_2\text{O}_{3-x}$  nanocrystals in the form of hollow spheres. Photocatalytic activity (PCA) was benchmarked against commercial  $\text{La}_2\text{O}_3$  and Evonik Aeroxide<sup>®</sup>  $\text{TiO}_2$  P25 via dye degradation experiments and a significant pH dependence of PCA is reported. Furthermore, chemical assays based on the Fenton reaction verified the scavenging properties of the synthesized materials towards reactive oxygen species (ROS), with increased scavenging of hydroxyl ( $\text{HO}^\bullet$ ) and superoxide ( $\text{O}_2^{\bullet-}$ ) radicals observed at pH 4.8. Biological assays (in vitro), with a 24 h incubation period in the presence of the  $\text{La}_2\text{O}_{3-x}$  nanoparticles, were conducted upon a non-malignant human keratinocyte cell line (HaCaT). The  $\text{La}_2\text{O}_{3-x}$  nanoparticles showed no toxicity when compared with the control over a significant concentration range. Biocompatibility with the non-malignant HaCaT cell line suggests the future application of  $\text{La}_2\text{O}_{3-x}$  as a doping material for inorganic oxides used as UV filters or as an antioxidant to mitigate oxidative stress by scavenging free radicals in conditions such as melanoma and inflammation.

## Graphic abstract



**Keywords** Spray pyrolysis · Oxygen deficient · Reactive oxygen species · Photodegradation · Radical scavenging

✉ Konstantin Konstantinov  
konstan@uow.edu.au

Extended author information available on the last page of the article

## Introduction

Reactive oxygen species (ROS) are essential for maintaining a healthy and normal life; however, an excessive production of ROS can cause irreversible damage to lipids, proteins, and DNA, leading to cell mutation and apoptosis. An excess of ROS has also been implicated in various neurodegenerative, respiratory, cancerous, and digestive disease conditions [1–3]. The excessive presence of ROS is indicative of an issue with the natural bodily antioxidant system [4, 5]. To support the underperforming antioxidant system, a material system with ROS scavenging/antioxidant properties is imperative. ROS scavenger materials can be organic or inorganic, and they function in different ways either by preventing or slowing down the autoxidation of the oxidisable molecules [6–11]. Inorganic oxide nanostructures have been a focus of current research because of their interesting and unique chemical and structural properties, unusual redox, and catalytic properties along with high surface area, chemical and mechanical stability, and biocompatibility [12–14]. Many metal oxide-based nanostructures are now essential constituents in cancer diagnosis and therapy, medical implants, neurochemical monitoring, cell labelling, and separation, and in targeted drug delivery [15–21]. The ROS scavenging capabilities of inorganic oxides depend upon the catalytic performance of metal oxide nanoparticles, which can be tailored by modifying the size, morphology, lattice defects, oxygen vacancies, and oxidation state of the material. This is particularly important in rare-earth (RE) metal oxides whereby the number of oxygen vacancies and oxidation state of the metal ion can influence its antioxidant behaviour [22, 23]. Also, considering the electronic configuration of RE elements, the outer shell 6s orbital is always filled and filling of the 4f shell increases with increasing atomic number, whilst the 5d<sup>1</sup> configuration appears in La, Ce, Gd, and Lu only [24–26]. The “lanthanide contraction” which is a progressive ionic radius contraction from La<sup>+3</sup> (1.08 Å) to Lu<sup>+3</sup> (0.85 Å) is also a unique feature of RE. Both electronic configuration and lanthanide contraction impart unique properties for their modern high tech applications [27–30].

Synthesis of biocompatible metal oxide nanostructures with oxygen and lattice defects by innovative and facile methods is crucial to exploit their properties for commercial applicability. Spray pyrolysis is a facile single-step synthesis process for producing nanostructures with controlled particle size and morphology. This is a continuous flow process with high yield, low cost, time saving, and high chemical flexibility. In addition, it can be performed in the absence of precipitating agents or surfactants and can produce highly crystalline materials without the need

for additional drying or calcination [31–33]. Briefly, this method involves the preparation of a precursor solution, which atomized through a nozzle into droplets and subsequently passed through a vertical heated furnace. The droplets undergo a series of physical phase changes within a quick succession including evaporation, precipitation, drying, thermal decomposition, and sintering. The final diameter of the spray pyrolysed particles can be roughly determined from the droplet size and the solute concentration in the solution. The morphology of the particles can be controlled by modifying various parameters such as the solution preparatory conditions, flow rate, precursor type, furnace temperature, relative vapour pressure, and additive chemistry in the solution [34, 35, 48].

Lanthanum (La), like cerium, is also an abundant RE element and finds use in a wide field of applications in the form of lanthanum oxide including: precision optical glasses, chemical catalysts [36–38], electrode materials, light-emitting materials, laser materials, and hydrogen storage materials. It is also being investigated for use in: targeted drug delivery within the body, fluorescence dyes, binding agent for several proteins, calcium channel suppression, and antimicrobial and phosphate removal agents based on the different nanoparticle morphologies that can be taken [39–42].

Considering the biocompatible nature of La<sub>2</sub>O<sub>3</sub> and its wide range of biological applications, it is worth to explore its role as a ROS scavenger. A limited research data is available on La<sub>2</sub>O<sub>3</sub> for targeted use in UV protection and as an antioxidant. Oxygen-deficient oxide nanostructures have proven efficient ROS scavengers and therapeutics. In this study, a novel spray pyrolysis synthesis method is employed to tailor the defect-rich oxygen-deficient (La<sub>2</sub>O<sub>3-x</sub>) nanostructure. The characterization, photodegradation chemical assays, and cytotoxicity study on non-malignant human keratinocyte cell line (HaCaT) of the synthesized structure are also presented to evaluate its potential application in the field of free radical scavenging in various disease conditions such as melanoma.

## Experimental methods

### Reagents used

Lanthanum oxide (La<sub>2</sub>O<sub>3</sub>, ≥ 99.9%, Sigma-Aldrich), nitric acid (HNO<sub>3</sub>, 68–70%, Sigma-Aldrich), iron sulphate heptahydrate (FeSO<sub>4</sub>·7H<sub>2</sub>O, ≥ 99%, Sigma-Aldrich), crystal violet (dimethylamino)phenyl methylium chloride) (C<sub>25</sub>H<sub>30</sub>N<sub>3</sub>Cl, ≥ 90%, Sigma-Aldrich), hydrochloric acid (HCl, 36.5–38%, Sigma-Aldrich), sodium acetate (C<sub>2</sub>H<sub>3</sub>NaO<sub>2</sub>, ≥ 99%, Sigma-Aldrich), citric acid (C<sub>6</sub>H<sub>6</sub>O<sub>7</sub>, ≥ 99.5%, Sigma-Aldrich), hydrogen peroxide (H<sub>2</sub>O<sub>2</sub>, 30% w/w, Sigma-Aldrich), AEROXIDE® TiO<sub>2</sub>

P25 (Evonik, denoted DP25), and zinc oxide nanopowder ( $\text{ZnO}$ ,  $\geq 97\%$ , Sigma-Aldrich,  $< 100$  nm) are purchased and used without any further treatment. Deionized (DI) water was used throughout the experiment for solution preparation.

## Synthesis of $\text{La}_2\text{O}_{3-x}$

For the synthesis of  $\text{La}_2\text{O}_{3-x}$  nanostructure by spray pyrolysis method, 2 g commercial lanthanum oxide ( $\text{La}_2\text{O}_3$ ) was mixed with 100 mL of DI water in a glass beaker. The solution was stirred on a magnetic stirrer for 30 min before 10 mL of concentrated  $\text{HNO}_3$  was added to dissolve the  $\text{La}_2\text{O}_3$ . After the complete dissolution of  $\text{La}_2\text{O}_3$ , the solution was sprayed through a spray pyrolysis system. The spray pyrolysis system consists of peristaltic pump, vertical tube furnace (height 1.4 m), collection chamber, and exhaust gas treatment unit shown in Fig. 1. The solution spray rate was maintained at  $7.5 \text{ mL min}^{-1}$  during the synthesis. Two samples were prepared by spraying the solution through the spray pyrolysis system at  $800^\circ\text{C}$  and  $950^\circ\text{C}$  temperature, respectively. Both samples were collected in an airtight glass vial and stored in a desiccator to avoid the slow spontaneous conversion into lanthanum hydroxide  $\text{La}(\text{OH})_3$  due to the hygroscopic nature of  $\text{La}_2\text{O}_3$ . The identification numbers and synthesis conditions for samples are given in Table 1.

## Characterization

The crystal phase composition of the prepared samples was characterized by X-ray diffraction (XRD, Enhanced Mini-Materials Analyser, MA, GBC scientific) with scanning angle  $2\theta$  ranging between 20 and 80 degree ( $^\circ$ ) at 40 kV and 20 mA, scan rate  $1.5^\circ \text{ min}^{-1}$ , and step size  $0.02^\circ$  using monochromatic  $\text{CuK}\alpha$  radiation ( $\lambda = 1.5405 \text{ \AA}$ ). The morphology of the samples was examined using the field-emission scanning electron microscopy (FE-SEM, JSM 7500F, JEOL). The samples were prepared for examination by coating the

**Table 1** Sample identification number (ID), synthesis method, and processing temperature

Sample ID	Synthesis/supplier	Processing temperature
C- $\text{La}_2\text{O}_3$	Commercial (Sigma-Aldrich)	As supplied
S800- $\text{La}_2\text{O}_3$	Spray pyrolysis	$800^\circ\text{C}$
S950- $\text{La}_2\text{O}_{3-x}$	Spray pyrolysis	$950^\circ\text{C}$

particles with platinum (Pt) on a carbon tape attached to aluminium (Al) base.

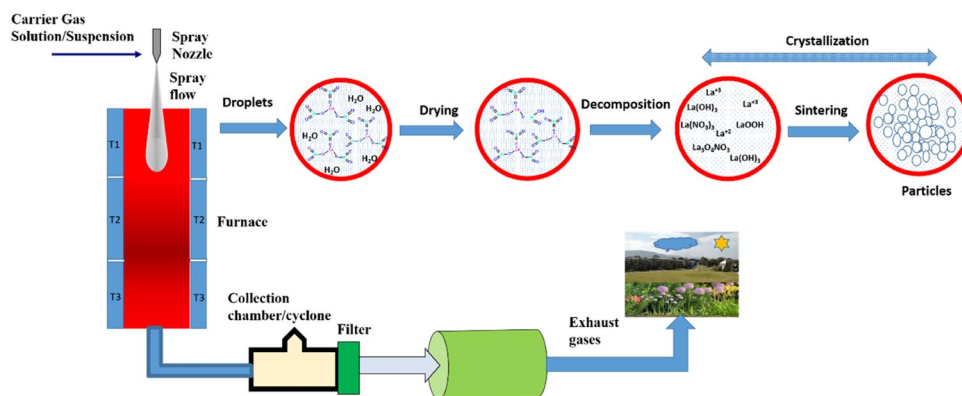
High-resolution transmission electron microscopy (TEM, JEM-ARM200F, JEOL) was also performed to analyse the crystal structure. The TEM specimens were prepared by drop-casting sample suspensions on carbon-coated copper grids and allowing to dry.

X-ray photoelectron spectroscopy (XPS) was conducted to further distinguish the phases based on shifts in binding energy. XPS was performed using the SPECS PHOIBOS 100 analyser installed in a high vacuum chamber with the base pressure below  $10^{-8}$  mbar, Al  $\text{K}\alpha$  radiations with photon energy  $h\nu = 1.487 \text{ keV}$  used as the X-ray excitation source at a high voltage of 12 kV and power of 120 W. The XPS spectra of binding energy were obtained at a pass energy of 20 eV in the fixed analyser transmission mode. Casa XPS software package version 2.3.15 was used to analyse the XPS data.

Thermo-gravimetric analysis (TGA) was performed to assess the mass loss due to the presence of hydroxide or nitrate phases. The measurements were taken by using TGA/DSC1, Mettler Toledo at a heating rate of  $5^\circ \text{ min}^{-1}$  in a continuous flow of air ( $100 \text{ mL min}^{-1}$ ) up to a temperature of  $830^\circ\text{C}$ . The percent mass loss was plotted against temperature for each sample.

Brunauer-Emmett-Teller (BET) surface area and Barret-Joyner-Halenda (BJH) pore size distribution were determined using the surface area and porosity analyser (Micromeritics Tristar II 3020). Before analysis, samples

**Fig. 1** Schematic of spray pyrolysis system and process mechanism



were dried for 24 h at 120 °C under vacuum in the sample tubes. All the measurements were performed at liquid nitrogen temperature, and the gaseous nitrogen (N<sub>2</sub>) was used as adsorbate.

UV–Vis absorption spectra were obtained from diffuse reflectance measurements performed on the powder samples in the 200–800 nm wavelength range using a UV-3600 spectrophotometer (Shimadzu) coupled with an integrating sphere attachment (ISR-3100, Shimadzu). The optical band gaps of the samples were determined from the Tauc plots obtained from the data based upon the following general expression [43, 44]:

$$(\alpha h\nu)^n = A(h\nu - E_g) \quad (1)$$

where  $\alpha$  is absorption coefficient,  $h$  is Planck's constant,  $\nu$  is the photon's frequency,  $A$  is the proportionality constant, and  $E_g$  is the optical band gap. The value of the exponent,  $n$ , depends upon the nature of the transition in the semiconductor material from conduction to valence band, and can vary between 0.5 and 3.

To assess the ROS scavenging and photocatalytic properties of the synthesized materials, crystal violet (CV) dye degradation was measured in the presence and absence of P25. The solution of C-La<sub>2</sub>O<sub>3</sub> and spray paralysed S950-La<sub>2</sub>O<sub>3-x</sub> were prepared by sonication. A separate suspension of P25 at a concentration of 5 mg L<sup>-1</sup> in DI water was also prepared. Aliquots of sample and P25 suspensions were transferred to a quartz beaker and diluted to 100 mL to yield final concentrations of 10 mg L<sup>-1</sup> and 5 mg L<sup>-1</sup>, respectively. The resultant suspension was then sonicated further for 5 min. Crystal violet solution (500 mg L<sup>-1</sup>) was added to the above-prepared solution. The suspension was then irradiated with UV light in a Rayonet UV photochemical reactor (RPR-200) for 60 min, with small aliquots collected every 10 min to assess the CV degradation by UV–Vis spectroscopy. P25 and CV were used as controls for the photodegradation and scavenging assay. The results of dye degradation were compared between irradiated and non-irradiated samples against controls by measuring the absorbance at  $\lambda = 590$  nm to determine the protective/scavenging mechanism of the La<sub>2</sub>O<sub>3-x</sub>.

A Fenton reaction-induced free radical scavenging assay was also performed to confirm the ROS scavenging properties of S950-La<sub>2</sub>O<sub>3-x</sub> nanostructure. Stock solutions of 50 mM of FeSO<sub>4</sub>·7H<sub>2</sub>O, 50 mg L<sup>-1</sup> of CV, 250 mg L<sup>-1</sup> scavenger solution (sample), and 0.1 M sodium acetate (C<sub>2</sub>H<sub>3</sub>NaO<sub>2</sub>) buffer (pH 3.5 and 4.8) were prepared. Test solutions  $\approx 10$  mL were made from the stock solutions of FeSO<sub>4</sub>·7H<sub>2</sub>O, C<sub>2</sub>H<sub>3</sub>NaO<sub>2</sub>, CV, H<sub>2</sub>O<sub>2</sub>, and DI water in the volume ratio 0.1, 0.8, 1, 1, and 7.1 mL, respectively. The pH of the test solution was adjusted by the addition of dilute HCL/NaOH solution.

Before the addition of H<sub>2</sub>O<sub>2</sub>, the solution was stirred for 2–3 min and an aliquot was collected as the zero control. Then, the required volume of H<sub>2</sub>O<sub>2</sub> was added to initiate the reaction and aliquots are collected at 05, 10, 20, 30, and 40 min to measure the absorbance at  $\lambda = 590$  nm. The same procedure was adopted in the presence of S950-La<sub>2</sub>O<sub>3-x</sub> and C-La<sub>2</sub>O<sub>3</sub> by mixing in a concentration 10 mg L<sup>-1</sup>.

## Cell culturing and in vitro cell viability assays

The adherent immortalized human keratinocyte cell line (HaCaT) used in this study was provided by Dr. J. Guy Lyons (University of Sydney). The identity of the cells was verified by “Short Tandem Repeat Profiling (Garvan Institute of Medical Research)”. The cell cultures were grown and maintained in T75 cm<sup>2</sup> tissue culture flasks (Greiner Bio-One) with Dulbecco's modified eagle medium (DMEM) supplemented with 10% (v/v) heat-inactivated fetal bovine serum (FBS, Bovogen Biologicals), 1% (v/v) penicillin/streptomycin (Thermo Fisher Scientific), and 2 mM GlutaMAX™ (Thermo Fisher Scientific). The T75 cm<sup>2</sup> with cell cultures were incubated at 37 °C with 5% (v/v) CO<sub>2</sub> and subculture every 3–4 days when the confluence level of the cells reached  $\geq 90\%$ . The cells were routinely checked for negative mycoplasma (MycAlert Mycoplasma Detection Kit, Lonza).

The viability of the HaCaT cell line was evaluated in the presence of nanoparticles using the MTS assay kit (CellTiter 96® Aqueous One Solution Cell Proliferation Assay Kit, Promega). In this assay, 100  $\mu$ L of the cells were seeded in a 96-well plate at a concentration 14–16  $\times 10^3$  cells/well and incubated at 37 °C with 5% (v/v) CO<sub>2</sub> for 24 h to adhere the cell to the bottom of the wells. The nanoparticles being tested on the HaCaT cell line were exposed first to UV light for 20 min, and then suspended in the same cell culturing media at concentration 500 mg L<sup>-1</sup> by sonication for 1 h. This suspension was further diluted to yield concentrations of 50 mg L<sup>-1</sup> and 5 mg L<sup>-1</sup>. The nanoparticle suspensions were added to the cells at concentration 0, 5, 50, and 500 mg L<sup>-1</sup> and incubated the cells further at 37 °C with 5% (v/v) CO<sub>2</sub> for 24 h. After 20 h of nanoparticles addition, a 20  $\mu$ L of MTS reagent was added to each well and waited for 4 h for colour development. After 48 h of total incubation time, the plate was centrifuged at 3000 RPM for 10 min and 75  $\mu$ L aliquots from each well were transferred to a new plate, and then, plate was read using a microplate reader (SpectraMax 384 Plus, Molecular Devices) at  $\lambda = 490$  nm. Each assay was performed in a set of three for each tested material and repeated in three separate experiments. The obtained data were plotted in the form of cell viability (% of control) for each sample concentration. Statistical data for the nanoparticles treatments and control were evaluated by one-way ANOVA Tuckey's post hoc test using the software



Prism 7.02 (GraphPad Software, USA). For analysis, value of  $p < 0.05$  was considered as significant.

## Results and discussion

XRD patterns of the synthesized samples (S800-La<sub>2</sub>O<sub>3</sub> and S950-La<sub>2</sub>O<sub>3-x</sub>) and commercial sample (C-La<sub>2</sub>O<sub>3</sub>) are shown in Fig. 2. Sample S800-La<sub>2</sub>O<sub>3</sub> did not fully converted into the oxide form, but rather exhibited a mixture of oxide, hydroxide, lanthanum nitrate, and lanthanum hydroxide nitrate due to the lower furnace temperature and fast processing during synthesis. Increasing the temperature up to 950 °C resulted in complete decomposition of the nitrate precursor into lanthanum oxide (Table 2).

The strongest peak for S950-La<sub>2</sub>O<sub>3-x</sub> appears at 30.16° and is assigned to the (011) plane of La<sub>2</sub>O<sub>3</sub>, whilst other peaks are assigned to the lattice planes (100), (002), (012), (110), (013), (200), (112), and (021), matching to the hexagonal crystalline phase of La<sub>2</sub>O<sub>3</sub> (PDF#04-008-7342), space group P-3m1 (164), and cell parameters:  $a = 3.9300$  Å,  $b = 3.9310$  Å, and  $c = 6.1200$  Å.

The average crystallite size is determined using Debye–Scherrer's equation [45, 46]:

$$D = \frac{k\lambda}{\beta \cos \theta} \quad (2)$$

where  $D$  = average crystallite size perpendicular to the reflecting planes (nm),  $k$  = shape factor (usually 0.9 for spherical crystallite),  $\lambda$  = X-ray wavelength (nm),  $\beta$  = full width half maximum (FWHM) of the peak (radians), and  $\theta$  = Bragg's angle (degree). The measured FWHM and crystallite size for all the samples are given in Table 2. Sample S950-La<sub>2</sub>O<sub>3-x</sub> showed smaller crystallite size of 24.80 nm as compared to C-La<sub>2</sub>O<sub>3</sub> (57.31 nm) and S800-La<sub>2</sub>O<sub>3</sub> (26.02 nm).

**Table 2** Constitutive substance/phases of lanthanum, FWHM, and crystallite size of C-La<sub>2</sub>O<sub>3</sub>, S800-La<sub>2</sub>O<sub>3</sub>, and S950-La<sub>2</sub>O<sub>3-x</sub>

Sample	Phases	FWHM (°)	Crystallite size (nm)
C-La <sub>2</sub> O <sub>3</sub>	La <sub>2</sub> O <sub>3</sub> + La(OH) <sub>3</sub>	0.3020	57.31
S800-La <sub>2</sub> O <sub>3</sub>	La <sub>2</sub> O <sub>3</sub> + La(OH) <sub>3</sub> + La(OH) <sub>2</sub> NO <sub>3</sub> + La(NO <sub>3</sub> ) <sub>3</sub>	0.4720	26.02
S950-La <sub>2</sub> O <sub>3-x</sub>	La <sub>2</sub> O <sub>3</sub>	0.4880	24.80

The peak shift was calculated based on the most intense peak of lattice plane (011) as shown in Fig. 2b. The reference (PDF#04-008-7342) peak from (011) plane exists at  $2\theta = 30.005^\circ$ , whilst for samples C-La<sub>2</sub>O<sub>3</sub> and S950-La<sub>2</sub>O<sub>3-x</sub>, it presents at  $2\theta = 30.07^\circ$  and  $2\theta = 30.16^\circ$ , respectively.

Major peak shift is observed in S950-La<sub>2</sub>O<sub>3-x</sub> as compared to C-La<sub>2</sub>O<sub>3</sub> with respect to the reference. In C-La<sub>2</sub>O<sub>3</sub>, the peak shift is caused by the presence of the hydroxide phase brought about by moisture absorption due to its hygroscopic nature. In the case of S950-La<sub>2</sub>O<sub>3-x</sub>, the observed peak shift can be linked to the vacancy doping and other structural defects.

The structural morphology of the samples (C-La<sub>2</sub>O<sub>3</sub>, S800-La<sub>2</sub>O<sub>3</sub>, and S950-La<sub>2</sub>O<sub>3-x</sub>) was studied by FE-SEM, as shown in Fig. 3. The structure of C-La<sub>2</sub>O<sub>3</sub> consists of agglomerates of irregular-shaped large particles. Due to irregular shape and large agglomerates, it is difficult to calculate the particle size for this sample. FE-SEM images for S800-La<sub>2</sub>O<sub>3</sub> and S950-La<sub>2</sub>O<sub>3-x</sub> depict round-shaped hollow particles of varying sizes. In the case of S800-La<sub>2</sub>O<sub>3</sub>, particle surfaces are intact and no cracking is observed, whereas S950-La<sub>2</sub>O<sub>3-x</sub> showed the crack initiation on the surface of the hollow spheres. The main reason for the particle surface disintegration is due to the fast heating, cooling conditions, and high temperature, as the spray pyrolysis sintering cycle is usually very short. The particle-size distributions of S800-La<sub>2</sub>O<sub>3</sub> and S950-La<sub>2</sub>O<sub>3-x</sub> are shown the Fig. 3d, e. The

**Fig. 2** (a) XRD pattern (b) and peaks shift with respect to reference pattern

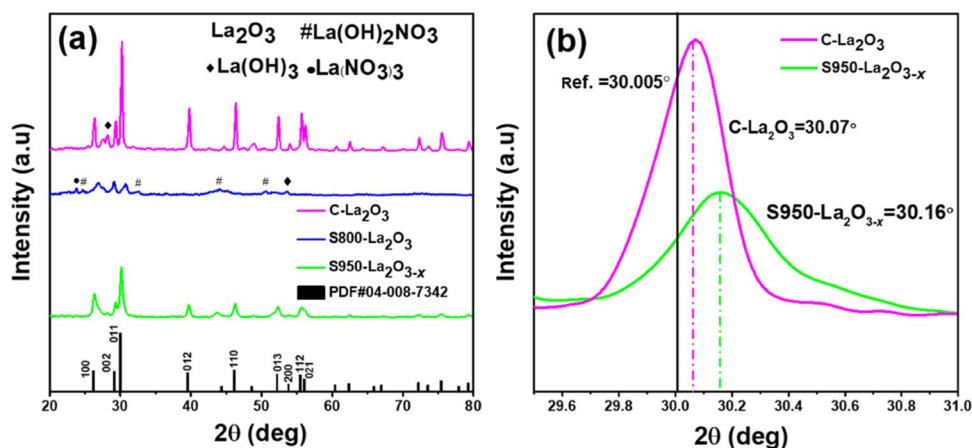
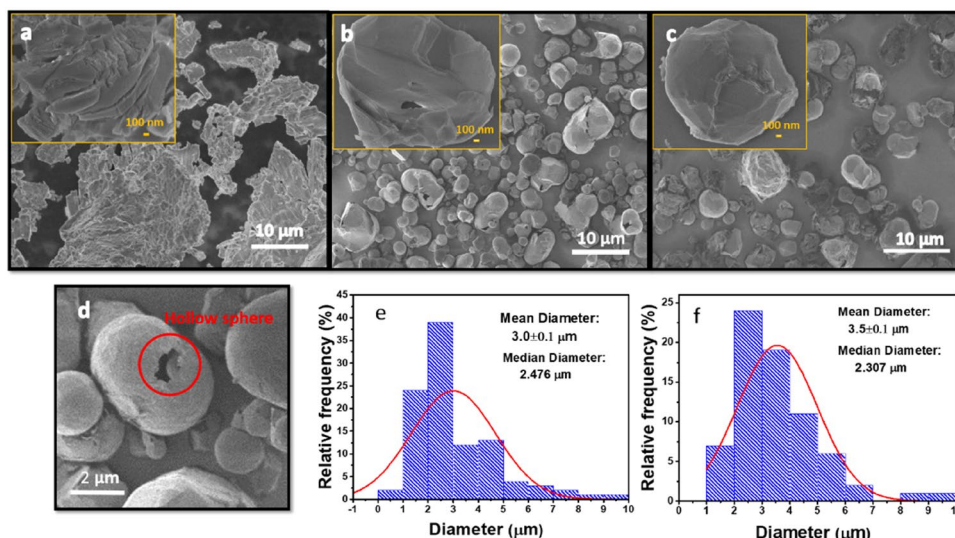


**Fig. 3** SEM images (a, b, and c) of C-La<sub>2</sub>O<sub>3</sub>, S800-La<sub>2</sub>O<sub>3</sub> and S950-La<sub>2</sub>O<sub>3-x</sub>, (d) hollow sphere morphology of S950-La<sub>2</sub>O<sub>3-x</sub>, and particle-size distribution (e) and (f) for S800-La<sub>2</sub>O<sub>3</sub> and S950-La<sub>2</sub>O<sub>3-x</sub>, respectively

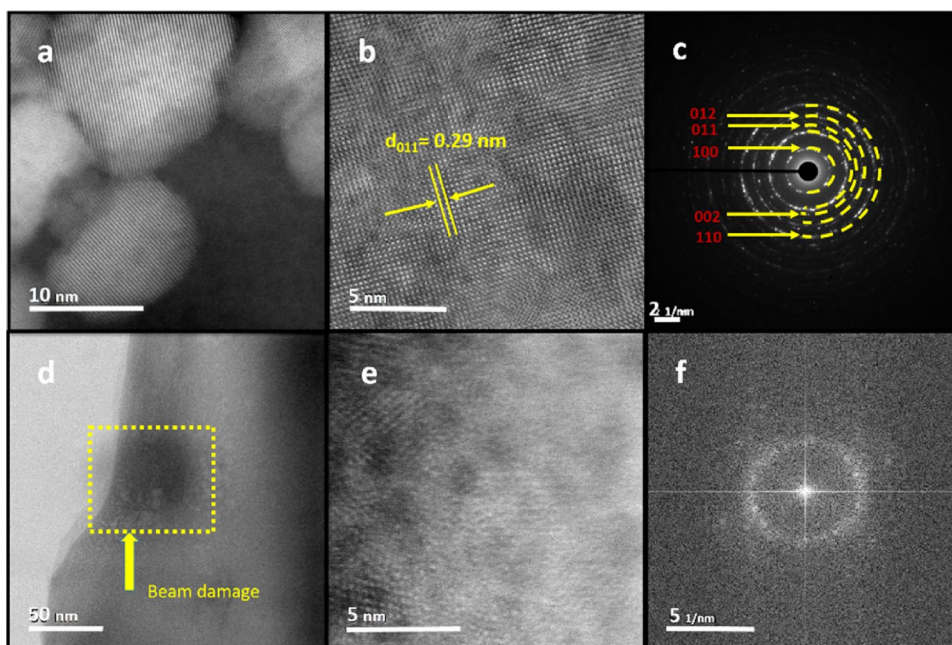


mean particle diameters of S800-La<sub>2</sub>O<sub>3</sub> and S950-La<sub>2</sub>O<sub>3-x</sub> are  $3.003 \pm 0.1 \mu\text{m}$  and  $3.549 \pm 0.1 \mu\text{m}$ , respectively. A hollow morphology of the spheres is usually obtained if the solution has less solute concentration. A rapid evaporation of volatiles due to the large temperature gradient causes supersaturation of the solute near the droplet surface. In short, a large temperature gradient, higher solute concentration on droplet surface, and rapid evaporation resulted in larger hollow spheres even with surface disintegration.

The HR-TEM images S800-La<sub>2</sub>O<sub>3</sub> and S950-La<sub>2</sub>O<sub>3-x</sub> are shown in Fig. 4a, d, respectively. TEM micrographs of S950-La<sub>2</sub>O<sub>3-x</sub> showed the presence of loosely held nanocrystals in large hollow spheres. It is linked to the fast chemical decomposition and reaction, where growth and sintering

of the crystals are impeded during the short cycle of spray pyrolysis. The soft porous aggregates of hollow sphere morphology were resulted due to initial droplet size and subsequent fast drying. These aggregates can be broken by sonication to form the suspension of the nanocrystals. The fast processing method also increased the chances of defect formation in the form of vacancies or oxygen deficiencies in the synthesized structure. The lattice d-spacing was calculated from the HR-TEM image, which is shown in Fig. 4b, c. The calculated value of d-spacing for S950-La<sub>2</sub>O<sub>3-x</sub> is 0.29 nm, corresponding to (011) lattice plane of the La<sub>2</sub>O<sub>3</sub> crystal phase. The selected area electron diffraction (SAED) pattern for S950-La<sub>2</sub>O<sub>3-x</sub> (Fig. 4c) depicts the lattice plane fringes for the La<sub>2</sub>O<sub>3</sub> crystal phase, corroborating with the XRD

**Fig. 4** HR-TEM micrographs and SAED pattern, (a, b,) and (c) of S950-La<sub>2</sub>O<sub>3-x</sub> and (d, e,) and (f) of S800-La<sub>2</sub>O<sub>3</sub>, respectively



results. On the other hand, it is difficult to resolve the atomic planes and to get the SAED pattern for S800-La<sub>2</sub>O<sub>3</sub> due to incomplete conversion of this sample into oxide as shown in Fig. 4e, f, respectively. TEM micrograph of S800-La<sub>2</sub>O<sub>3</sub>, Fig. 4d, showed the beam damage during analysis, which confirmed the presence of lanthanum hydroxide La(OH)<sub>3</sub> in the sample.

The presence of hydroxide and nitrate impurities in the samples was also confirmed by TGA measurements shown in Fig. 5. In case of C-La<sub>2</sub>O<sub>3</sub>, about 3.8% weight loss was observed over 40–830 °C thermal range, linked to the minute water absorption at the surface as evidenced by the hydroxide impurity observed in XRD pattern of the respective sample. For S950-La<sub>2</sub>O<sub>3-x</sub>, about 5.8% weight loss was resulted over the entire thermal range with no sharp drop in mass, linked to the combined effect of drying and sintering of nitrate or hydroxide traces, although XRD did not show any prominent evidence of hydroxide or nitrate phase in this sample. A major weight-loss event is observed in S800-La<sub>2</sub>O<sub>3</sub> between 460 and 590 °C temperatures. This is the transition period for the formation of different nitrate-based phases from lanthanum nitrate: La(NO<sub>3</sub>)<sub>3</sub> → LaONO<sub>3</sub> → La<sub>3</sub>O<sub>4</sub>NO<sub>3</sub> [47, 48]. Also, La(OH)<sub>3</sub> converts into lanthanum hydroxide oxide (LaOOH) at ≈330 °C, and further decomposes into pure oxide La<sub>2</sub>O<sub>3</sub> phase at temperatures above 490 °C [49]. Both these decomposition events are linked to the observed mass loss, which further validates the mixed-phase composition of S800-La<sub>2</sub>O<sub>3</sub> suggested from the XRD and TEM results.

To further analyse surface defects and verify the XRD results of the commercial and synthesized samples, XPS was carried out. The binding energy (BE) of the obtained XPS spectra was corrected using the C 1 s peak reference value

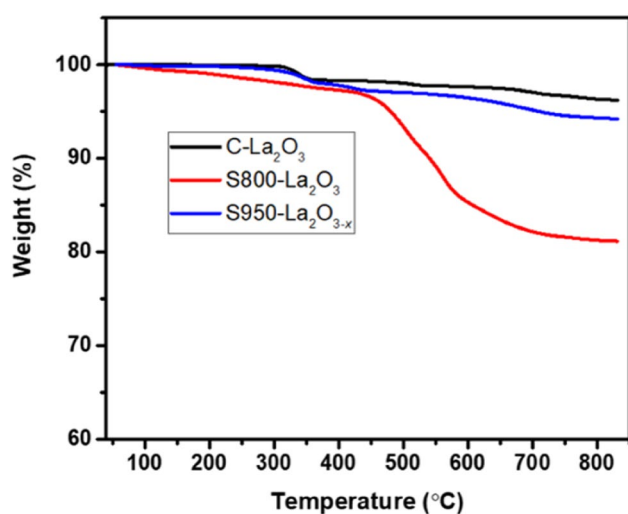


**Fig. 5** Thermo-gravimetric analysis of samples (C-La<sub>2</sub>O<sub>3</sub>, S800-La<sub>2</sub>O<sub>3</sub>, and S950-La<sub>2</sub>O<sub>3-x</sub>)

of 284.8 eV. The positions after peak deconvolution and fitting of La 3d (La 3d<sub>5/2</sub>, 3d<sub>3/2</sub>) and O 1 s regions of C-La<sub>2</sub>O<sub>3</sub>, S800-La<sub>2</sub>O<sub>3</sub>, and S950-La<sub>2</sub>O<sub>3-x</sub> are shown in Fig. 6, and their respective BE values given in Table 3.

When comparing the deconvoluted 3d region (3d<sub>5/2</sub> and 3d<sub>3/2</sub> doublets) spectra, C<sub>0</sub>, C<sub>1</sub>, and C<sub>2</sub> peaks of S950-La<sub>2</sub>O<sub>3-x</sub> are present at lower binding energies than respective peaks of S800-La<sub>2</sub>O<sub>3</sub> and C-La<sub>2</sub>O<sub>3</sub> (Table 3). According to literature, separation between bonding (C<sub>1</sub>) and antibonding (C<sub>2</sub>) peaks/satellites increases from the hydroxide/mixed phase to the pure oxide phase, and relative intensities of these peaks exhibit a similar trend due to strong hybridization in the oxide phase [50–52]. Sample S950-La<sub>2</sub>O<sub>3-x</sub> showed greater separation between the bonding and antibonding peaks as compared to C-La<sub>2</sub>O<sub>3</sub> and S800-La<sub>2</sub>O<sub>3</sub>. Hence, the analysis of 3d region proves that S950-La<sub>2</sub>O<sub>3-x</sub> has defect-rich oxide phase structure.

Deconvolution of the O 1s region for each sample shows the presence of two peaks O1 (larger peak) and O2 (smaller peak), Fig. 6. For C-La<sub>2</sub>O<sub>3</sub>, peak O1 is at 531.56 eV BE, conforms to the BE values of lanthanum hydroxide (ref. ~531.4 eV) [50, 51, 53] and peak O2 at a BE of 529.26 eV as a broader spectrum shows the presence of oxide phase (ref. ~528.4–530.5 eV) [50, 51, 53]. The peak O1 for S800-La<sub>2</sub>O<sub>3</sub> is at BE 532.01 eV which can be attributed to the hydroxide nature of the sample. This sample did not fully decompose into the oxide phase due to lower processing temperature, and consists of a mixture of lanthanum hydroxide, oxide, and nitrate phases. The peak O2 present at BE 528.15 eV appeared as a shoulder off the main O1 peak, which represents the oxide phase, possibly due to a thin layer/fine crystals at the surface. The peak O1 for S950-La<sub>2</sub>O<sub>3-x</sub> is present at BE 530.08 eV, which is lower than the observed BE values of C-La<sub>2</sub>O<sub>3</sub> and S800-La<sub>2</sub>O<sub>3</sub> and conforms to the reported BE values of lanthanum oxide in the literature. The peak O2 present at BE 532.75 eV, can be attributed to adsorbed moisture, hydroxyl groups, or oxygen-rich surface [51, 53]. However, XRD pattern does not show prominent hydroxide peak in the spectra. The presence of this peak can also be linked to the formation of defect state in the oxide phase due to the different coordinated position of the oxygen atoms. The existence of O2 peak at higher BE is already reported in the literature, linked to the structural defects/variation from the standard reference values [50]. XPS results successfully distinguished the oxide and hydroxide nature of the samples based on the BE values in the deconvoluted spectra and also verified the XRD results.

N<sub>2</sub> adsorption–desorption isotherms and corresponding pore size distributions by BJH analysis are shown in Fig. 7 for C-La<sub>2</sub>O<sub>3</sub>, S800-La<sub>2</sub>O<sub>3</sub>, and S950-La<sub>2</sub>O<sub>3-x</sub>, respectively. All three isotherms can be classified as Type-III isotherms, with no monolayer coverage but a multilayer coverage. Almost no hysteresis is observed, and the isotherms opening



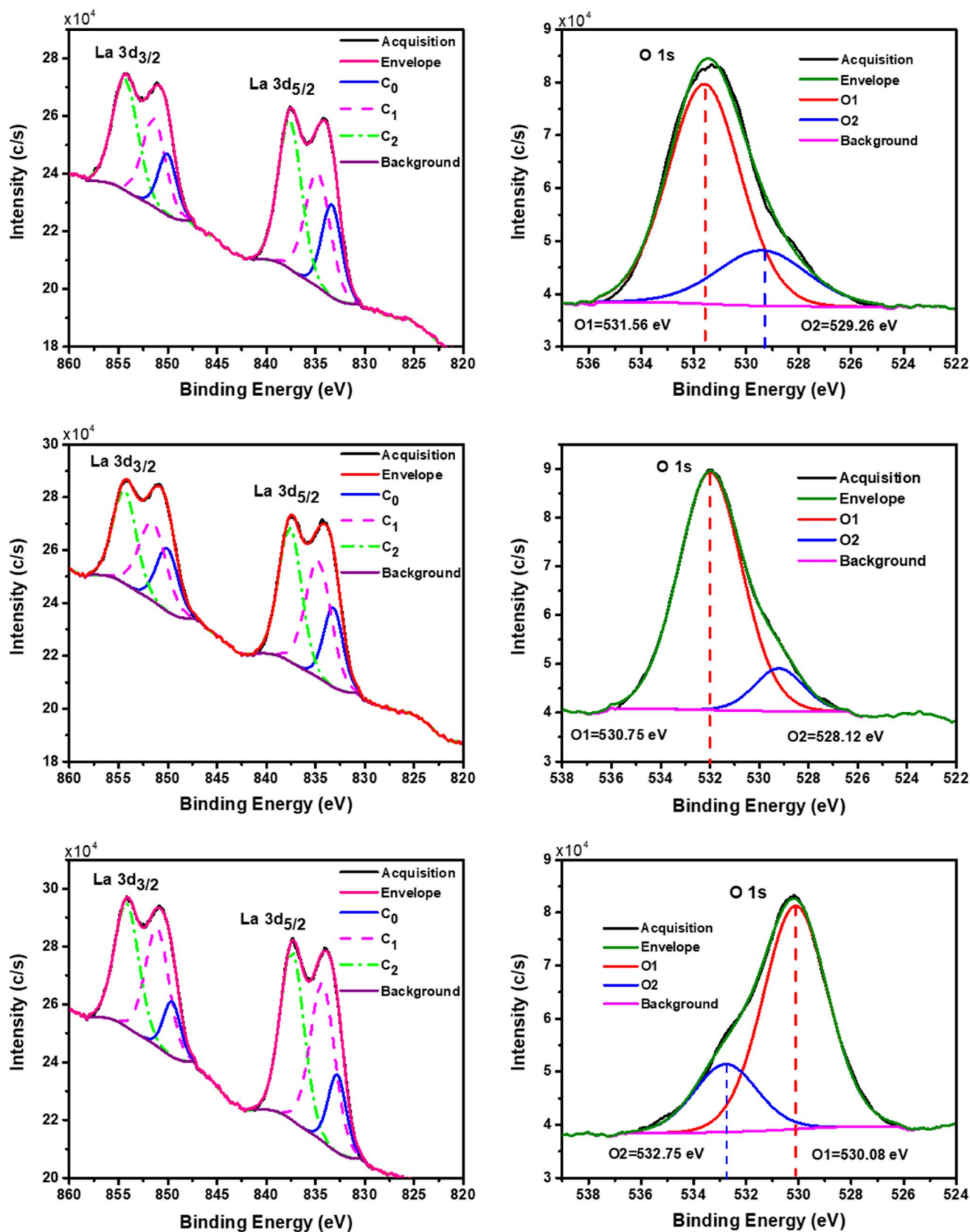
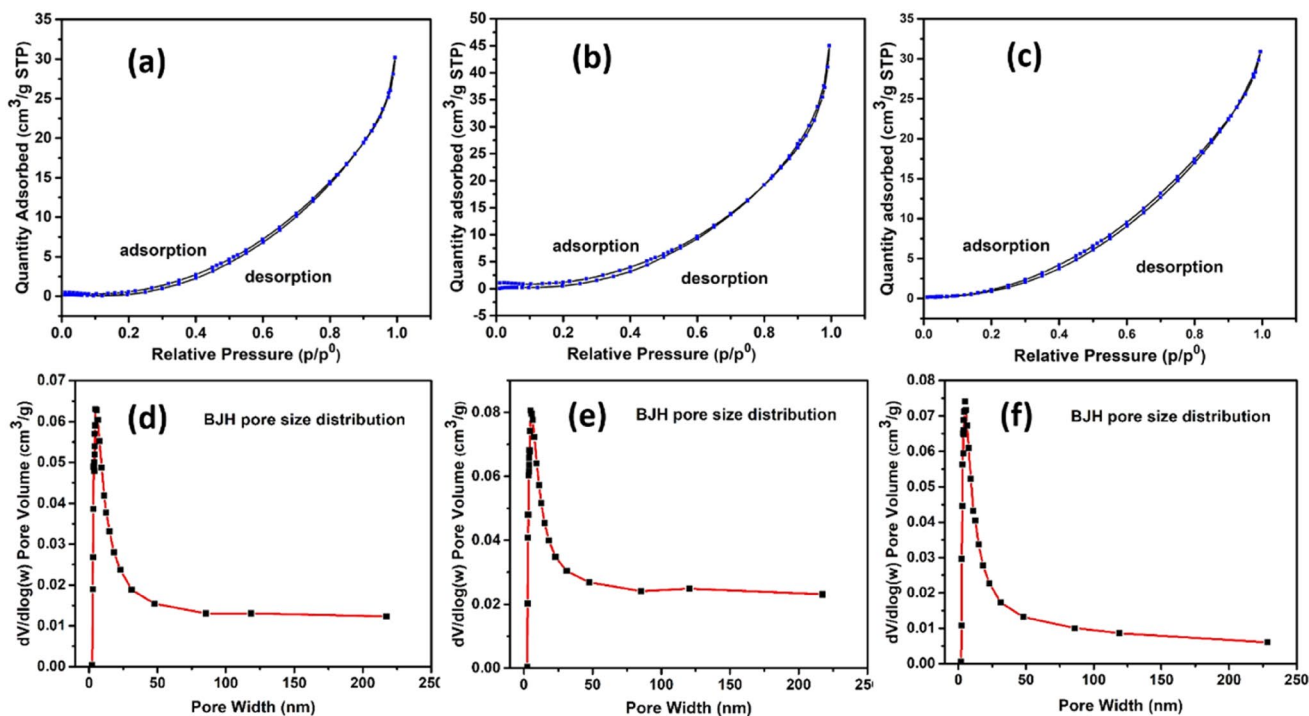


Fig. 6 XPS spectra after peak deconvolution of 3d and O1s regions of (a) C-La<sub>2</sub>O<sub>3</sub>, (b) S800-La<sub>2</sub>O<sub>3</sub>, and (c) S800-La<sub>2</sub>O<sub>3-x</sub>, respectively



**Table 3** Binding energies of the deconvoluted  $3d_{5/2}$ ,  $3d_{3/2}$ , and O 1s regions, where  $C_0$  = without charge transfer,  $C_1$  = with charge transfer (antibonding), and  $C_2$  = with charge transfer (bonding) from the ligand

	Binding energy (eV)							
	$3d_{5/2}$			$3d_{3/2}$			O 1s	
	$C_0$	$C_1$	$C_2$	$C_0$	$C_1$	$C_2$	$O_1$	$O_2$
C-La <sub>2</sub> O <sub>3</sub>	833.28	834.76	837.49	850.01	851.31	854.32	531.56	529.26
S800-La <sub>2</sub> O <sub>3</sub>	833.51	834.85	837.51	850.12	851.58	854.38	532.01	529.21
S950-La <sub>2</sub> O <sub>3-x</sub>	832.78	834.21	837.21	849.56	851.01	854.02	530.08	532.75



**Fig. 7** BET N<sub>2</sub> sorption and desorption isotherms (a, b, c), and BJH pore size distribution (d, e, f) for C-La<sub>2</sub>O<sub>3</sub>, S800-La<sub>2</sub>O<sub>3</sub>, and S950-La<sub>2</sub>O<sub>3-x</sub>, respectively

towards lower pressure in case of C-La<sub>2</sub>O<sub>3</sub> and S800-La<sub>2</sub>O<sub>3</sub> indicate the presence of porous particles/aggregates and more macropores, whereas in case of S950-La<sub>2</sub>O<sub>3-x</sub>, the isotherm closes towards lower pressure suggesting the absence/small volume of macropores and presence of rigid particles/aggregates. BJH analysis of the pore size distribution indicates the presence of mesopores > 90% along with the presence of some macropores in S950-La<sub>2</sub>O<sub>3-x</sub>. The absence of micropores also confirmed the multilayer coverage in the N<sub>2</sub> adsorption–desorption isotherm. The BET surface area, BJH average pore width and BJH cumulative pore volume are given in Table 4. A higher cumulative pore volume (0.0860 cm<sup>3</sup>g<sup>-1</sup> and smaller average pore width (7.05 nm) of S950-La<sub>2</sub>O<sub>3-x</sub> in comparison to C-La<sub>2</sub>O<sub>3</sub> and S800-La<sub>2</sub>O<sub>3</sub> confirmed its more porous nature and hence porous aggregate of nanocrystals.

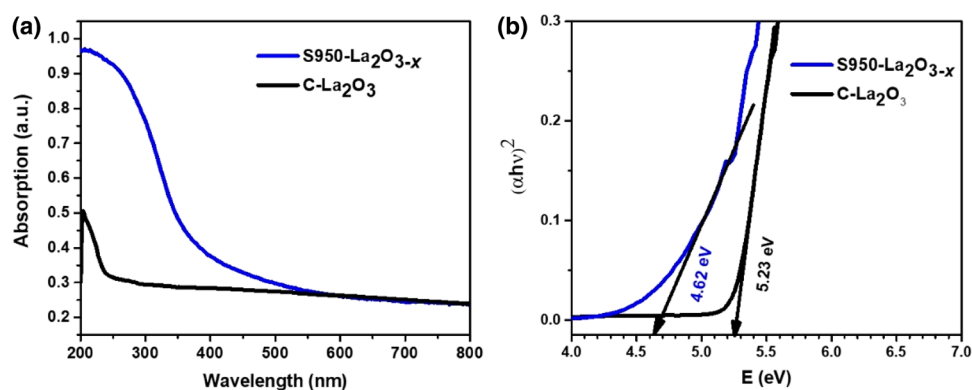
**Table 4** BET surface area, average pore width, and BJH cumulative volume of samples

Sample	BET surface area (m <sup>2</sup> g <sup>-1</sup> )	Average pore width (nm) (BJH)	BJH cumulative pore volume (cm <sup>3</sup> g <sup>-1</sup> ), adsorption
C-La <sub>2</sub> O <sub>3</sub>	3.7234	8.32	0.0635
S800-La <sub>2</sub> O <sub>3</sub>	19.1301	9.15	0.0598
S950-La <sub>2</sub> O <sub>3-x</sub>	16.1266	7.05	0.0860

The characterization of the samples has clearly demonstrated the formation of single-phase hollow spheres consisting of nanocrystals in S950-La<sub>2</sub>O<sub>3-x</sub> at 950 °C, whereas lower temperature (800 °C) precursor did not decompose completely into oxide phase. To further assess the UV absorption and ROS scavenging properties, it is very



**Fig. 8** **a** UV–Vis absorption spectra and **b** band-gap determination by Tauc plot



meaningful to consider the single-phase S950-La<sub>2</sub>O<sub>3-x</sub> only in comparison with the commercial C-La<sub>2</sub>O<sub>3</sub>.

Diffuse reflectance measurements were performed so as to ascertain the optical absorption properties of the samples, Fig. 8(a). Sample S950-La<sub>2</sub>O<sub>3-x</sub> showed higher UV absorption in 200–360 nm range than the C-La<sub>2</sub>O<sub>3</sub>. The optical band gaps calculated from the Tauc plots (Fig. 8b) were determined to be 5.23 and 4.62 eV for C-La<sub>2</sub>O<sub>3</sub> and S950-La<sub>2</sub>O<sub>3-x</sub>, respectively. The decrease in the band gap of S950-La<sub>2</sub>O<sub>3-x</sub> suggests the presence of defect state in the structure. Based on the composition dependence electronic structure, vacancy-induced defect state is formed at or near the conduction band edge in large band semiconductor materials [54]. Hence, an enhanced UV–Vis absorption for S950-La<sub>2</sub>O<sub>3-x</sub> was observed.

For the UV photodegradation experiments, two controls, CV and CV + P25 were used to compare the photodegradation of CV caused by the photo-mediated production of ROS to that of the samples and, hence, evaluate the ROS scavenging role of the S950-La<sub>2</sub>O<sub>3-x</sub> nanostructure. In the presence of CV only, S950-La<sub>2</sub>O<sub>3-x</sub> showed no significant dye degradation even after 1 h exposure, and similar trend shown by C-La<sub>2</sub>O<sub>3</sub>, in comparison with the control. Hence, it could be suggested that samples are not/least generating free radical species or constituting any electron transfer to

degrade the dye solution. The other way around, the synthesized sample may provide a protection against free radical generation, i.e., may scavenge free radicals. The second set of UV–Vis photodegradation experiments were performed in the presence of P25 photocatalyst. Degradation results for the control (CV + P25) and in the presence of C-La<sub>2</sub>O<sub>3</sub> and S950-La<sub>2</sub>O<sub>3-x</sub> nanoparticles are plotted in Fig. 9(a). Sample C-La<sub>2</sub>O<sub>3</sub> did not show any protection to the dye solution against P25 photocatalysis, whereas S950-La<sub>2</sub>O<sub>3-x</sub> demonstrated the highest protection/free radical scavenging when compared with the control. This sample consists of nanocrystals of single-phase La<sub>2</sub>O<sub>3-x</sub>, in the aggregate of hollow spheres with retarded crystal growth and vacancies. The rate constants of the chemical reactions were determined from the plot of irradiation time (min) and ln(C<sub>0</sub>/C) as shown the Fig. 9(b). These are pseudo-first-order rate reactions described by the Langmuir–Hinshelwood model [55]. Rate constants (*k*) min<sup>-1</sup> were determined from the linear plot of ln(C<sub>0</sub>/C) vs irradiation time using the expression [55, 56]:

$$\ln\left(\frac{C_0}{C}\right) = kt \quad (3)$$

**Fig. 9** UV–Vis photodegradation plots **a** change in relative absorbance vs incubation time (min) and **b** degradation kinetics

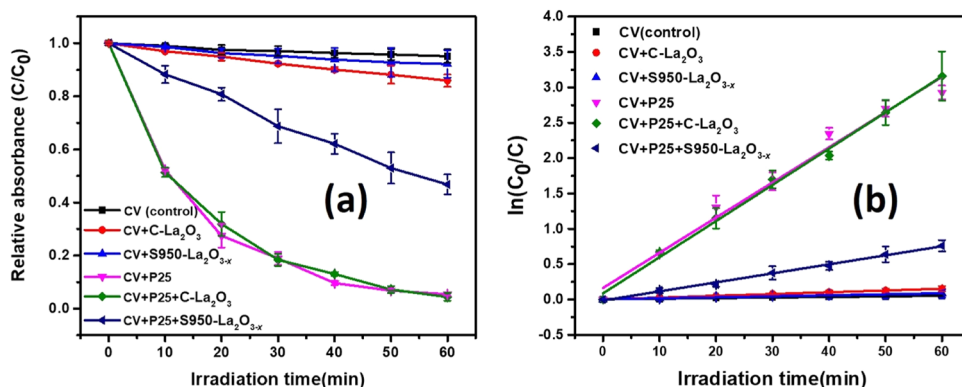


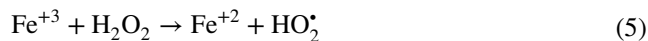
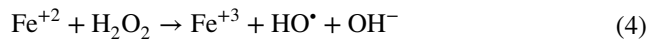
**Table 5** Degradation reaction rate constant ( $k$ ) with standard error obtained by linear fit of data

Sample	Rate constant $k$ ( $\text{min}^{-1}$ )	Standard error
CV(Control)	$8.22 \times 10^{-4}$	$6.68 \times 10^{-5}$
CV + C-La <sub>2</sub> O <sub>3</sub>	$2.5 \times 10^{-3}$	$4.56 \times 10^{-5}$
CV + S950-La <sub>2</sub> O <sub>3-x</sub>	$1.43 \times 10^{-3}$	$9.45 \times 10^{-5}$
CV + P25	$4.97 \times 10^{-2}$	$3.11 \times 10^{-3}$
CV + P25 + C-La <sub>2</sub> O <sub>3</sub>	$5.11 \times 10^{-2}$	$1.44 \times 10^{-3}$
CV + P25 + S950-La <sub>2</sub> O <sub>3-x</sub>	$1.27 \times 10^{-2}$	$3.63 \times 10^{-4}$

where  $t$  is the irradiation time (min),  $C_0$  is the initial concentration, and  $C$  is the concentration at different irradiation times ( $\text{mg L}^{-1}$ ). In comparison to the control (CV only), assay (P25 + CV), and C-La<sub>2</sub>O<sub>3</sub> + P25 + CV have highest rate constant as shown in Table 5.

In reduced pH environment, ROS are highly reactive towards protein, DNA, and lipids causing significant destruction of cells. High concentration of protons (down to pH 5.4) and ROS ( $\sim 1 \text{ mM H}_2\text{O}_2$ ) have been reported in the inflamed tissues [57, 58]. To optimize pH conditions according to inflamed tissues for efficient ROS scavenging, a chemical assay was performed at pH 3.5 and 4.8. The assay is based on Fenton reaction and performed in the presence of  $\text{H}_2\text{O}_2$  and  $\text{FeSO}_4 \cdot 7\text{H}_2\text{O}$  in the acidic environment at the

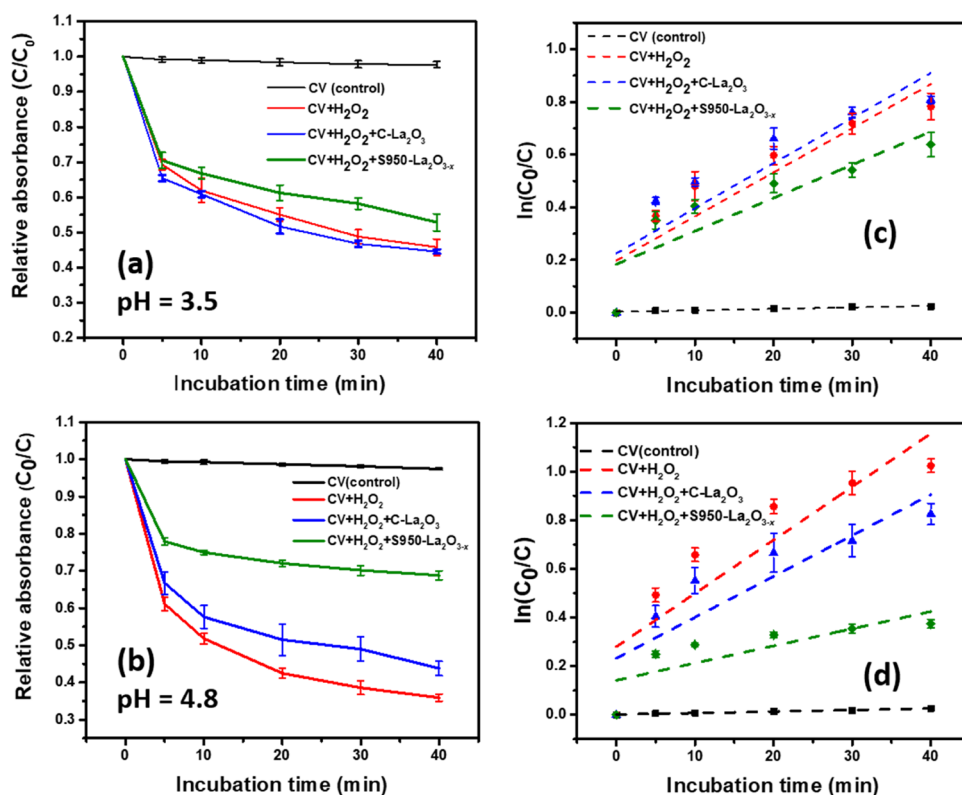
mentioned pH values. The combination of  $\text{Fe}^{+2}$  and  $\text{H}_2\text{O}_2$  results in the formation of ROS ( $\cdot\text{OH}$ , and  $\text{HO}_2\cdot$ ) through the following reactions [59, 60]:



The second reaction ( $\text{Fe}^{+3} + \text{H}_2\text{O}_2$ ) is quite slow in comparison to the first reaction ( $\text{Fe}^{+2} + \text{H}_2\text{O}_2$ ), which results in the depletion of an iron ( $\text{Fe}^{+2}$ ) source necessary for sustaining the Fenton reaction. Free radicals generated during the reaction react with the dye and cause its degradation. The use of a free radical scavenger prevents/decreases the reaction of the free radicals with organic matter by exploiting its scavenging properties.

ROS scavenging capability based on dye degradation assay at pH = 3.5 and 4.8 is shown in Fig. 10. Without the presence of scavenger and  $\text{H}_2\text{O}_2$ , no dye degradation was observed as shown by the control (CV only) at both pH values, 3.5 and 4.8 in Fig. 10a, b. After inclusion of  $\text{H}_2\text{O}_2$  into the test solution, maximum degradation was observed as shown by the trend line for CV +  $\text{H}_2\text{O}_2$ . The degradations kinetics in the presence of C-La<sub>2</sub>O<sub>3</sub> and S950-La<sub>2</sub>O<sub>3-x</sub> in comparison with control are shown by the assay CV +  $\text{H}_2\text{O}_2$  + C-La<sub>2</sub>O<sub>3</sub> and CV +  $\text{H}_2\text{O}_2$  + S950-La<sub>2</sub>O<sub>3-x</sub> in Fig 10c, d, respectively.

**Fig. 10** Fenton reaction-based chemical assays, **a** pH 3.5 and **b** pH 4.8, and with corresponding reaction kinetics (**c, d**), respectively

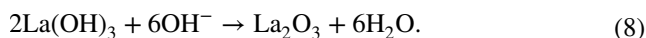
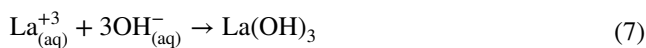


It was observed that at pH 3.5, no significant ROS scavenging was observed. However, at pH = 4.8, a significant ROS scavenging effect was observed as shown in Fig. 10b. Sample S950-La<sub>2</sub>O<sub>3-x</sub> showed the highest ROS scavenging at pH = 4.8 as compared to the C-La<sub>2</sub>O<sub>3</sub>. Also it is noted that after 20 min of incubation, S950-La<sub>2</sub>O<sub>3-x</sub> continue to scavenge free radicals without any decrease in dye absorbance. Sample C-La<sub>2</sub>O<sub>3</sub> also showed some ROS scavenging effect possibly due to interconversion reactions of La<sub>2</sub>O<sub>3</sub> and La(OH)<sub>3</sub> (Eq. 7 and Eq. 8, respectively), and this phenomenon can also be considered in S950-La<sub>2</sub>O<sub>3-x</sub>, but higher scavenging effect of this sample is imparted by the structural defects due to the processing conditions. Generally, it can be observed from the graph that after 5 min of H<sub>2</sub>O<sub>2</sub> inclusion, ROS generation rate is higher than ROS scavenging rate and, hence, more dye degradation observed. As H<sub>2</sub>O<sub>2</sub> is consumed with passage of time, rate of ROS generation and scavenging balanced.

The presence of vacancies (oxygen deficiency, defects) usually facilitates the free radical scavenging. As a result of the imbalanced conditions of spray pyrolysis, it is highly likely to develop a defect-rich La<sub>2</sub>O<sub>3-x</sub> structure [61]. The oxygen vacancy formation requires the removal of neutral oxygen atom by breaking the metal–oxygen bond and redistribution of electrons after bond breakage [54, 62]. There is tendency of La<sub>2</sub>O<sub>3-x</sub> to change into stable form La<sub>2</sub>O<sub>3</sub> by exposing the structure La<sub>2</sub>O<sub>3-x</sub> to radiations, temperature, suitable pH, and solution conditions:



These electrons reduce the hydroxyl radical (<sup>•</sup>OH) into water. Whereas the holes (h<sup>+</sup>) act as the charge neutralizer sites during the scavenging assay. The La<sup>+3</sup> ion further reacts with OH<sup>-</sup> to yield La(OH)<sub>3</sub> and subsequently a reverse reaction of La(OH)<sub>3</sub> with OH<sup>-</sup> to yield La<sub>2</sub>O<sub>3</sub> [63, 64]:



The second reaction kinetics is strongly dependent on pH of the reaction media, as we noticed a higher ROS scavenging at pH 4.8 than pH 3.5.

The chemical assay clearly demonstrated efficient ROS scavenging down to pH 4.8, lowering the pH below 4.8 value quickly quenched the vacancies and rapidly converted the La<sub>2</sub>O<sub>3</sub> to La(OH)<sub>3</sub>, whereas at pH ≥ 4.8, vacancies undergo slow conversion by means of chemical interaction with ROS along with the transformation of La<sub>2</sub>O<sub>3</sub> to La(OH)<sub>3</sub>. Hence, the assay showed that S950-La<sub>2</sub>O<sub>3-x</sub> nanoparticles can effectively scavenge free radicals in the inflamed tissues in milieu

to their reduced pH, and act as a potent therapeutic to reduce oxidative stress.

The HaCaT cell line was chosen for cytotoxic study, as it is composed of keratinocytes, the major cell type of the epidermis, and the superficial layer of skin in intimate contact with environmental contaminants. Also, exposure to UV radiations generates excessive ROS that causes oxidative damage to the skin, which may lead to inflammation, premature aging, and melanoma [43, 65, 66]. Cytotoxic study will help to evaluate the suitability of the synthesized material for use in skin products to provide protection and therapy.

Cell cytotoxic assay was performed using the pristine ZnO nanoparticles, C-La<sub>2</sub>O<sub>3</sub>, and synthesized S950-La<sub>2</sub>O<sub>3-x</sub> nanoparticles at 500, 50, and 5 mg L<sup>-1</sup>, as shown in Fig. 11. The percentage of viable cells incubated with S950-La<sub>2</sub>O<sub>3-x</sub> nanoparticles at the tested concentrations (500, 50, and 5 mg L<sup>-1</sup>) does not vary significantly to the viable cells (control) determined without nanoparticles. Sample C-La<sub>2</sub>O<sub>3</sub> showed no significant cytotoxic effect at concentrations 50 and 5 mg L<sup>-1</sup>, whereas a cell mortality about 20% of the control was observed at the higher concentration 500 mg L<sup>-1</sup>. The difference in cytotoxicity at higher concentration (500 mg L<sup>-1</sup>) is linked to the morphological difference and structural defects between S950-La<sub>2</sub>O<sub>3-x</sub> and C-La<sub>2</sub>O<sub>3</sub>. Also, it was observed that the spherical particles of

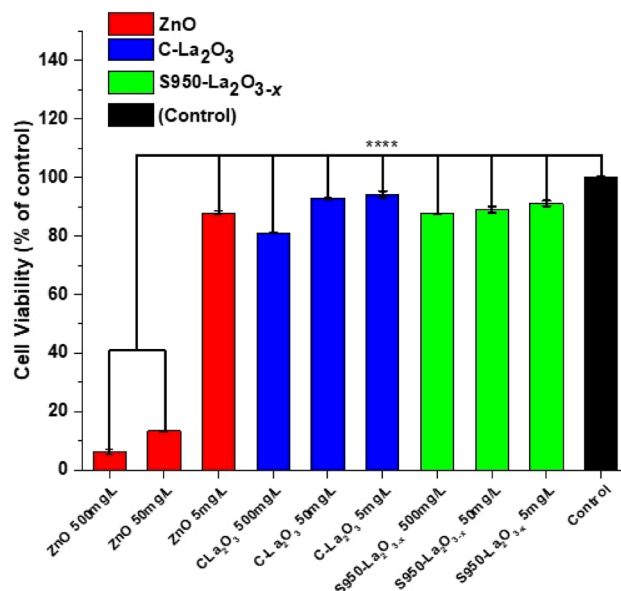


**Fig. 11** HaCaT cell viability after 24 h incubation with nanoparticles of ZnO, C-La<sub>2</sub>O<sub>3</sub>, and spray pyrolysed S950-La<sub>2</sub>O<sub>3-x</sub> at concentration 5, 50, and 500 mg L<sup>-1</sup>. Cell viability (% of control) refers to normalized absorbance values for each concentration. Data represent mean ± SD of three experiments (*n* = 3 per experiment). One-way ANOVA and Tukey post hoc tests were performed to check the statistically different data sets, where \*\*\*\* indicates *p* < 0.0001, when comparing to the control only data sets, cell viability data sets of ZnO at 50 and 500 mg L<sup>-1</sup> are significantly different from the other data sets



spray pyrolysed S950-La<sub>2</sub>O<sub>3-x</sub> consist of nanocrystals, easily suspended into the cell culture media compared to C-La<sub>2</sub>O<sub>3</sub> upon sonication. Cell viability data sets for C-La<sub>2</sub>O<sub>3</sub> and S950-La<sub>2</sub>O<sub>3-x</sub> at all concentrations (500, 50, and 5 mg L<sup>-1</sup>) are significant to ZnO data sets at 500 and 50 mg L<sup>-1</sup> concentrations.

## Conclusion

La<sub>2</sub>O<sub>3-x</sub> nanostructure was successfully synthesized by simple and low-cost spray pyrolysis method without any surfactant, precipitating agent, or supporting material. The synthesized structures were characterized by XRD, XPS, SEM, HR-TEM, TGA, and UV–Vis spectroscopy.

A hollow sphere-like morphology consisting of nanocrystals in the oxygen-deficient oxide (La<sub>2</sub>O<sub>3-x</sub>) nanostructure was obtained at 950 °C as revealed by SEM and TEM characterization. XPS studies confirmed the formation of defects/oxygen vacancies in the nanostructure. Defects in S950-La<sub>2</sub>O<sub>3-x</sub> nanostructure caused band gap (4.62 eV) reduction as compared to the commercial C-La<sub>2</sub>O<sub>3</sub> (5.23 eV), which hence increased UV–Vis absorption shown by the S950-La<sub>2</sub>O<sub>3-x</sub>. Photodegradation experiments showed no degradation of dye in the presence of the synthesized particles and dye only, whereas photodegradation in the presence of P25 showed the potential ROS scavenging properties of the nanostructure due to less dye degradation as compared to the P25 only. Furthermore, as a supplementary evidence, a pH-dependent chemical assay based on Fenton reaction in the absence of UV light confirmed the potential scavenging effect of the spray pyrolysed single-phase S950-La<sub>2</sub>O<sub>3-x</sub> structure. At pH 4.8, after 40 min of incubation time, ~20% less dye degradation was observed as compared to pH 3.5.

Furthermore, the cytotoxicity data of the S950-La<sub>2</sub>O<sub>3-x</sub> nanostructure towards HaCaT cell line even at high concentration have demonstrated its biocompatible nature.

Hence, the photocatalytic degradation, and chemical and biological assay results of the synthesized S950-La<sub>2</sub>O<sub>3-x</sub> nanostructure potentiate its useful applications for the treatment/prevention of various ROS-related disease conditions. In case of skin-related disease such as ROS-driven tumour (melanoma), the nanostructure is an ideal therapeutic for mitigation and prevention of disease. Further study on synthesis process, ROS scavenging control will advance its role as a biocompatible additive with antioxidant properties, UV protection, and suppression of organic degradation.

**Acknowledgements** This research work is a part of University of Wollongong (UOW) Global challenge program “Next Generation Sunscreens”, carried out at the Institute of Super Conducting and Electronic Materials (ISEM), Australian Institute for Innovative Materials (AIIM), and the Illawarra Health & Medical Research Institute (IHMRI), UOW. In addition, the financial support also provided under

the joint scholarship program of Higher education commission (HEC) Pakistan and UOW, Australia. We would like to thank Dr. Dongqi Shi (ISEM, UOW) for his assistance in XPS measurements. Furthermore, the authors acknowledge the use of Electron Microscopy facility (EMC), AIIM, at University of Wollongong, Australia.

## Compliance with ethical standards

**Conflict of interest** The authors declare no conflict of interest.

## References

- Skulachev, V.P.: Mitochondria-targeted antioxidants as promising drugs for treatment of age-related brain diseases. *J. Alzheimers Dis.* **28**(2), 283–289 (2012)
- Trachootham, D., Alexandre, J., Huang, P.: Targeting cancer cells by ROS-mediated mechanisms: a radical therapeutic approach? *Nat. Rev. Drug. Discov.* **8**(7), 579 (2009)
- Puspita, L., Chung, S.Y., Shim, J.-W.: Oxidative stress and cellular pathologies in Parkinson’s disease. *Mol. Brain* **10**(1), 53 (2017)
- Sies, H.: Oxidative stress: a concept in redox biology and medicine. *Redox Biol.* **4**, 180–183 (2015)
- Schieber, M., Chandel, N.S.: ROS function in redox signaling and oxidative stress. *Curr. Biol.* **24**(10), R453–R462 (2014)
- Ingold, K.U., Pratt, D.A.: Advances in radical-trapping antioxidant chemistry in the 21st century: a kinetics and mechanisms perspective. *Chem. Rev.* **114**(18), 9022–9046 (2014)
- Cadet, J., Wagner, J.R.: Oxidatively generated base damage to cellular DNA by hydroxyl radical and one-electron oxidants: similarities and differences. *Arch. Biochem. Biophys.* **557**, 47–54 (2014)
- Zhang, H., Forman, H.J.: 4-hydroxynonenal-mediated signaling and aging. *Free Radic. Biol. Med.* **111**, 219–225 (2017)
- Morry, J., Ngamcherdrakul, W., Yantasee, W.: Oxidative stress in cancer and fibrosis: Opportunity for therapeutic intervention with antioxidant compounds, enzymes, and nanoparticles. *Redox Biol.* **11**, 240–253 (2017)
- Valgimigli, L., Baschieri, A., Amorati, R.: Antioxidant activity of nanomaterials. *J. Mater. Chem. B* **6**(14), 2036–2051 (2018)
- Thannickal, V.J., Fanburg, B.L.: Reactive oxygen species in cell signaling. *Am. J. Physiol. Lung Cell Mol. Physiol.* **279**(6), L1005–L1028 (2000)
- Jeong Kim, T., Seok Chae, K., Chang, Y., Ho Lee, G.: Gadolinium oxide nanoparticles as potential multimodal imaging and therapeutic agents. *Curr. Top. Med. Chem.* **13**(4), 422–433 (2013)
- Yin, J., Chen, D., Zhang, Y., Li, C., Liu, L., Shao, Y.: MRI relaxivity enhancement of gadolinium oxide nanoshells with a controllable shell thickness. *Phys. Chem. Chem. Phys.* **20**(15), 10038–10047 (2018)
- Salem, R., Thurston, K.G., Carr, B.I., Goin, J.E., Geschwind, J.-F.H.: Yttrium-90 microspheres: radiation therapy for unresectable liver cancer. *J. Vasc. Interv. Radiol.* **13**(9), S223–S229 (2002)
- Campbell, C.T., Peden, C.H.: Oxygen vacancies and catalysis on ceria surfaces. *Science* **309**(5735), 713–714 (2005)
- Suh, W.H., Suslick, K.S., Stucky, G.D., Suh, Y.-H.: Nanotechnology, nanotoxicology, and neuroscience. *Prog. Neurobiol.* **87**(3), 133–170 (2009)
- Song, H.-T., Choi, J.-S., Huh, Y.-M., Kim, S., Jun, Y.-W., Suh, J.-S., Cheon, J.: Surface modulation of magnetic nanocrystals in the development of highly efficient magnetic resonance probes for intracellular labeling. *J. Am. Chem. Soc.* **127**(28), 9992–9993 (2005)



18. Silva, G.A.: Neuroscience nanotechnology: progress, opportunities and challenges. *Nat. Rev. Neurosci.* **7**(1), 65 (2006)
19. Faraji, A.H., Wipf, P.: Nanoparticles in cellular drug delivery. *Bioorg. Med. Chem.* **17**(8), 2950–2962 (2009)
20. Rehman, F., Zhao, C., Jiang, H., Wang, X.: Biomedical applications of nano-titania in theranostics and photodynamic therapy. *Biomater. Sci.* **4**(1), 40–54 (2016)
21. Chen, Y.-W., Moussi, J., Drury, J.L., Wataha, J.C.: Zirconia in biomedical applications. *Expert Rev. Med. Devic.* **13**(10), 945–963 (2016)
22. Dunnick, K.M., Pillai, R., Pisane, K.L., Stefaniak, A.B., Sabolsky, E.M., Leonard, S.S.: The effect of cerium oxide nanoparticle valence state on reactive oxygen species and toxicity. *Biol. Trace Elem. Res.* **166**(1), 96–107 (2015)
23. Pulido-Reyes, G., Rodea-Palomares, I., Das, S., Sakthivel, T.S., Leganes, F., Rosal, R., Seal, S., Fernández-Piñas, F.: Untangling the biological effects of cerium oxide nanoparticles: the role of surface valence states. *Sci. Rep.* **5**, 15613 (2015)
24. Hirosaki, N., Ogata, S., Kocer, C.: Ab initio calculation of the crystal structure of the lanthanide  $\text{Ln}_2\text{O}_3$  sesquioxides. *J. Alloys Compd.* **351**(1–2), 31–34 (2003)
25. Zinkevich, M.: Thermodynamics of rare earth sesquioxides. *Prog. Mater. Sci.* **52**(4), 597–647 (2007)
26. Morozov, N.N., Morozov, E.: The heat capacity, thermodynamic functions, and 4f-electron states of rare-earth compounds: Rare-earth oxides of the A type. *High Temp.* **38**(5), 705–714 (2000)
27. Panichev, A.: Rare earth elements: review of medical and biological properties and their abundance in the rock materials and mineralized spring waters in the context of animal and human geophagia reasons evaluation. *Achiev. Life Sci.* **9**(2), 95–103 (2015)
28. Nieminen, M., Putkonen, M., Niinistö, L.: Formation and stability of lanthanum oxide thin films deposited from  $\beta$ -diketonate precursor. *Appl. Surf. Sci.* **174**(2), 155–166 (2001)
29. Sanivarapu, S.R., Lawrence, J.B., Sreedhar, G.: Role of surface oxygen vacancies and lanthanide contraction phenomenon of  $\text{Ln}(\text{OH})_3$  (Ln= La, Pr, and Nd) in sulfide-mediated photoelectrochemical water splitting. *ACS Omega* **3**(6), 6267–6278 (2018)
30. Seitz, M., Oliver, A.G., Raymond, K.N.: The lanthanide contraction revisited. *J. Am. Chem. Soc.* **129**(36), 11153–11160 (2007)
31. Cho, J.S., Kang, Y.C.: Nano-sized hydroxyapatite powders prepared by flame spray pyrolysis. *J. Alloys Compd.* **464**(1–2), 282–287 (2008)
32. Ozcelik, B.K., Ergun, C.: Synthesis and characterization of iron oxide particles using spray pyrolysis technique. *Ceram. Int.* **41**(2), 1994–2005 (2015)
33. Ozcelik, B.K., Ergun, C.: Synthesis of ZnO nanoparticles by an aerosol process. *Ceram. Int.* **40**(5), 7107–7116 (2014)
34. Lenggoro, I.W., Hata, T., Iskandar, F., Lunden, M.M., Okuyama, K.: An experimental and modeling investigation of particle production by spray pyrolysis using a laminar flow aerosol reactor. *J. Mater. Res.* **15**(3), 733–743 (2000)
35. Lenggoro, I.W., Okuyama, K., de la Mora, J.F., Tohge, N.: Preparation of ZnS nanoparticles by electrospray pyrolysis. *J. Aerosol Sci.* **31**(1), 121–136 (2000)
36. Hu, C., Liu, H., Dong, W., Zhang, Y., Bao, G., Lao, C., Wang, Z.L.:  $\text{La}(\text{OH})_3$  and  $\text{La}_2\text{O}_3$  nanobelts—synthesis and physical properties. *Adv. Mater.* **19**(3), 470–474 (2007)
37. Nowicki, W., Rypka, G., Kawalko, A., Tolińska, A., Kirszenstejn, P.: Synthesis and characterization of  $\text{SiO}_2$ – $\text{La}_2\text{O}_3$  gels obtained in a water-free environment. *J. Mater. Sci.* **49**(13), 4416–4422 (2014)
38. Klingenberg, B., Vannice, M.A.: Influence of pretreatment on lanthanum nitrate, carbonate, and oxide powders. *Chem. Mater.* **8**(12), 2755–2768 (1996)
39. Tang, T., Deng, H.Q., Jiang, Q.Y., Huo, J.C., Hu, S.H.: Preparation of Bismuth-Lanthanum composite oxide and its photocatalytic performance. *Adv. Mater. Res.* **616**, 1667–1670 (2013)
40. Kafadaryan, Y., Petrosyan, S., Badalyan, G., Lazaryan, V., Shirinyan, G., Aghamalyan, N., Hovsepyan, R., Semerjian, H., Igityan, A., Kuzanyan, A.: Structural characteristics of  $\text{La}_2\text{O}_3$  thin film grown on  $\text{LaB}_6$ . In: *Int. J. Mod. Phys.: Conference Series* 2012, vol. **15**, pp. 61–66. World Scientific.
41. Liu, J., Wang, G., Lu, L., Guo, Y., Yang, L.: Facile shape-controlled synthesis of lanthanum oxide with different hierarchical micro/nanostructures for antibacterial activity based on phosphate removal. *RSC Adv.* **7**(65), 40965–40972 (2017)
42. Wang, K., Wu, Y., Li, H., Li, M., Guan, F., Fan, H.: A hybrid antioxidizing and antibacterial material based on Ag– $\text{La}_2\text{O}_3$  nanocomposites. *J. Inorg. Biochem.* **141**, 36–42 (2014)
43. Morlando, A., Borrás, M.C., Rehman, Y., Bakand, S., Barker, P., Sluyter, R., Konstantinov, K.: Development of  $\text{CeO}_2$  nanodot encrusted  $\text{TiO}_2$  nanoparticles with reduced photocatalytic activity and increased biocompatibility towards a human keratinocyte cell line. *J. Mater. Chem. B* **8**(18), 4016–4028 (2020)
44. Escobedo-Morales, A., Ruiz-López, I., Ruiz-Peralta, M.D., Tepach-Carrillo, L., Sánchez-Cantú, M., Moreno-Orea, J.: Automated method for the determination of the band gap energy of pure and mixed powder samples using diffuse reflectance spectroscopy. *Heliyon* **5**(4), e01505 (2019)
45. Bindu, P., Thomas, S.: Estimation of lattice strain in ZnO nanoparticles: X-ray peak profile analysis. *J. Theor. Appl. Phys.* **8**(4), 123–134 (2014)
46. Muhammed Shafi, P., Chandra Bose, A.: Impact of crystalline defects and size on X-ray line broadening: A phenomenological approach for tetragonal  $\text{SnO}_2$  nanocrystals. *AIP Adv.* **5**(5), 057137 (2015)
47. Mentus, S., Jelić, D., Grudić, V.: Lanthanum nitrate decomposition by both temperature programmed heating and citrate gel combustion. *J. Therm. Anal. Calorim.* **90**(2), 393–397 (2007)
48. Leng, J., Wang, Z., Wang, J., Wu, H.-H., Yan, G., Li, X., Guo, H., Liu, Y., Zhang, Q., Guo, Z.: Advances in nanostructures fabricated via spray pyrolysis and their applications in energy storage and conversion. *Chem. Soc. Rev.* **48**(11), 3015–3072 (2019)
49. Neumann, A., Walter, D.: The thermal transformation from lanthanum hydroxide to lanthanum hydroxide oxide. *Thermochim. Acta* **445**(2), 200–204 (2006)
50. Sunding, M., Hadidi, K., Diplas, S., Løvrvik, O., Norby, T., Gunnæs, A.: XPS characterisation of in situ treated lanthanum oxide and hydroxide using tailored charge referencing and peak fitting procedures. *J. Electron Spectros. Relat. Phenomena* **184**(7), 399–409 (2011)
51. Li, J.P.H., Zhou, X., Pang, Y., Zhu, L., Vovk, E.I., Cong, L., van Bavel, A.P., Li, S., Yang, Y.: Understanding of binding energy calibration in XPS of lanthanum oxide by in situ treatment. *Phys. Chem. Chem. Phys.* **21**(40), 22351–22358 (2019)
52. Maiti, D., Daza, Y.A., Yung, M.M., Kuhn, J.N., Bhethanabotla, V.R.: Oxygen vacancy formation characteristics in the bulk and across different surface terminations of  $\text{La}_{(1-x)}\text{Sr}_x\text{Fe}_{(1-y)}\text{Co}_y\text{O}_{(3-\delta)}$  perovskite oxides for  $\text{CO}_2$  conversion. *J. Mater. Chem. A* **4**(14), 5137–5148 (2016)
53. Stoychev, D., Valov, I., Stefanov, P., Atanasova, G., Stoycheva, M., Marinova, T.: Electrochemical growth of thin  $\text{La}_2\text{O}_3$  films on oxide and metal surfaces. *Mater. Sci. Eng. C* **23**(1–2), 123–128 (2003)
54. Ganduglia-Pirovano, M.V., Hofmann, A., Sauer, J.: Oxygen vacancies in transition metal and rare earth oxides: Current state of understanding and remaining challenges. *Surf. Sci. Rep.* **62**(6), 219–270 (2007)
55. Konstantinou, I.K., Albanis, T.A.:  $\text{TiO}_2$ -assisted photocatalytic degradation of azo dyes in aqueous solution: kinetic and



- mechanistic investigations: a review. *Appl. Catal. B Environ.* **49**(1), 1–14 (2004)
56. Colon, J., Herrera, L., Smith, J., Patil, S., Komanski, C., Kupelian, P., Seal, S., Jenkins, D.W., Baker, C.H.: Protection from radiation-induced pneumonitis using cerium oxide nanoparticles. *Nanomed-Nanotechnol.* **5**(2), 225–231 (2009)
57. Mariotto, S., de Prati, A.C., Cavalieri, E., Amelio, E., Marlinghaus, E., Suzuki, H.: Extracorporeal shock wave therapy in inflammatory diseases: molecular mechanism that triggers anti-inflammatory action. *Curr. Med. Chem.* **16**(19), 2366–2372 (2009)
58. Pu, H.-L., Chiang, W.-L., Maiti, B., Liao, Z.-X., Ho, Y.-C., Shim, M.S., Chuang, E.-Y., Xia, Y., Sung, H.-W.: Nanoparticles with dual responses to oxidative stress and reduced pH for drug release and anti-inflammatory applications. *ACS Nano* **8**(2), 1213–1221 (2014)
59. Xie, J., Wang, Z., Lu, S., Wu, D., Zhang, Z., Kong, H.: Removal and recovery of phosphate from water by lanthanum hydroxide materials. *Chem. Eng. J.* **254**, 163–170 (2014)
60. Neyens, E., Baeyens, J.: A review of classic Fenton's peroxidation as an advanced oxidation technique. *J. Hazard Mater.* **98**(1–3), 33–50 (2003)
61. Patnaik, P.: *Handbook of inorganic chemicals*, vol. 529. McGraw-Hill, New York (2003)
62. Gunawan, C., Lord, M.S., Lovell, E., Wong, R.J., Jung, M.S., Oscar, D., Mann, R., Amal, R.: Oxygen-vacancy engineering of cerium-oxide nanoparticles for antioxidant activity. *ACS Omega* **4**(5), 9473–9479 (2019)
63. Kulperger, R., Okun, R., Munford, G.: Methods and compositions using lanthanum for removing phosphate from water. In. U.S. Patent No. 6,524,487. 25 Feb. (2003)
64. Reddy, S.S., Berchmans, L.J., Sreedhar, G.: Imperfect oriented attachment of lanthanum hydroxide nanoparticles. *CrystEng-Comm* **21**(25), 3829–3835 (2019)
65. Uy, B., McGlashan, S.R., Shaikh, S.B.: Measurement of reactive oxygen species in the culture media using Acridan Lumigen PS-3 assay. *J. Biomol. Tech. JBT* **22**(3), 95 (2011)
66. Liu, L., Xie, H., Chen, X., Shi, W., Xiao, X., Lei, D., Li, J.: Differential response of normal human epidermal keratinocytes and HaCaT cells to hydrogen peroxide-induced oxidative stress. *Clin. Exp. Dermatol. Exp. Dermatol.* **37**(7), 772–780 (2012)

**Publisher's Note** Springer Nature remains neutral with regard to jurisdictional claims in published maps and institutional affiliations.

## Affiliations

Yaser Rehman<sup>1</sup> · Corentin Copet<sup>2</sup> · Alexander Morlando<sup>1</sup> · Xu-Feng Huang<sup>3</sup> · Konstantin Konstantinov<sup>1</sup> 

<sup>1</sup> Institute for Superconducting and Electronics Materials (ISEM), University of Wollongong (UOW), Wollongong, NSW 2522, Australia

<sup>2</sup> University of Clermont Auvergne, 63000 Clermont-Ferrand, France

<sup>3</sup> Illawarra Health and Medical Research Institute (IHMRI), University of Wollongong (UOW), Wollongong, NSW 2522, Australia

